A Digital Current Controller Based on Active Resistance Term Feedback for SPMSM Drives

Xin Yuan, *Member, IEEE*, Jie Mei, *Member, IEEE*, Jiahao Chen, *Member, IEEE*, Yuefei Zuo, *Member, IEEE*, and Christopher H. T. Lee, *Senior Member, IEEE*

***Abstract*—Improving the control performance of surfaced-mounted permanent magnet synchronous machine (SPMSM) drives, digital current controllers with active resistance term feedback (ARTF) based on an exact zero-order hold (ZOH) equivalent discrete SPMSM model have been developing. Derived from the ARTF structure, few approaches are developed to suppress the ARTF delay effect on the digital current controller. To fill this gap, an improved digital current controller with the proposed digital internal mode control current estimator is designed. In the proposed structure, the predicted current can be effectively utilized as the ARTF delay compensation and feedback of the current controller at the same time. Compared with other state-of-the-art digital current controllers with ARTF, the performance evaluation of dynamic response, disturbance rejection, and parameter robustness is originally carried out based on the exact ZOH equivalent discrete SPMSM model. Furthermore, the experimental results are able to fully verify the correctness of the proposed method.**

***Index Terms*—Active resistance term feedback (ARTF), internal mode control (IMC), parameter robustness, surfaced-mounted permanent magnet synchronous machine (SPMSM).**

NOMENCLATURE

U_{dq}, i_{dq}	dq-axis stator voltage and current.
U'_{dq}	dq-axis distorted voltage caused by inverter nonlinearity.
U^{ref}_{dq}	dq-axis inverter reference voltage.
ω_e, θ_e	Electrical angular speed and angle.
L_s, R_s	Actual stator inductance and resistance.
ψ_m, ψ	Actual and initial rotor flux linkage.
L, R	Initial inductance and resistance in controller.
U^{ref}_s	$\alpha\beta$-axis inverter reference voltage.
U'_s, ψ_s	$\alpha\beta$-axis distorted voltage caused by inverter nonlinearity and stator flux linkage.
T_s	Digital system sampling period.
i^{ref}_{dq}	dq-axis reference stator current.

Manuscript received November 20, 2021; revised January 13, 2022; accepted February 17, 2022. Date of publication February 24, 2022; date of current version April 28, 2022. This work was supported by the National Research Foundation (NRF) Singapore, under its NRF Fellowship Grant NRF-NRFF12-2020-0003. Recommended for publication by Associate Editor J. Ye. *(Corresponding author: Christopher H. T. Lee.)*

Xin Yuan, Jiahao Chen, Yuefei Zuo, and Christopher H. T. Lee are with the School of Electrical and Electronic Engineering, Nanyang Technological University, Singapore 639798 (e-mail: xin.yuan@ntu.edu.sg; horychen@qq.com; zuoyuefei@ujs.edu.cn; chtlee@ntu.edu.sg).

Jie Mei is with the Department of Electrical Engineering and Computer Science, Massachusetts Institute of Technology, Cambridge, MA 02139 USA (e-mail: jiemei@mit.edu).

Color versions of one or more figures in this article are available at https://doi.org/10.1109/TPEL.2022.3153057.

Digital Object Identifier 10.1109/TPEL.2022.3153057

I. INTRODUCTION

In surfaced-mounted permanent magnet synchronous machine (SPMSM) current control, researchers have developed several current control schemes. One of the most popular schemes is proportional–integral (PI) current control, which not only can keep zero steady-state current error performance but also possess disturbance rejection [1]–[3]. Owning fast dynamic responses, predictive current control has been getting wide attention, but it is more sensitive to parameter mismatch between controller and machine [4]–[6].

Generally, PI current controller was employed to control dq-axis torque and flux currents (i_q, i_d) of SPMSM and the flux current is set to zero or negative value for flux-weakening. Due to the involvement of rotor flux linkage and cross-coupling inductance terms in SPMSM model, a state-feedback decoupling PI current controller was developed [7], [8]. Based on this controller, the feedback variables can cancel the imaginary part of the plant pole. In order to reduce the inductance parameter sensitivity, a complex vector PI current controller was designed in the 1998s [9]. The main point is that the complex plant pole is directly canceled by a matching zero provided by the current controller. To enhance disturbance rejection of current controllers, active resistance term feedback (ARTF) is designed. Utilizing ARTF, the plant pole location is forced to move left [10].

Motivated by the development of digital systems such as advanced RISC machines (ARM) and digital signal processors (DSP) microprocessors, digital current controllers have been getting more increasing attention. Generally, digital PI current controllers using forward Euler transform have been established [11], [12]. The basic procedure is to transform the designed controller model from continuous-time domain (s domain) to discrete-time domain. However, it has been noted that the digital implementation of continuous-time derived PI current controller can worsen the performance when the current regulator is tuned for high bandwidth or the operating condition is under high fundamental excitation frequencies relative to the sampling frequencies [13]–[15]. Regarding solving this issue, an improved predictive current control based on a fully discretized SPMSM model is proposed [16]. However, a complex nonlinear disturbance observer with d-axis current injection method needs

to be designed to suppress the disturbance caused by parameter mismatch in the predictive current control. In order to avoid the design of disturbance observers, a digital PI current controller considering computation delay model is proposed [17], [18]. Furthermore, without employing forward Euler transform, a digital current controller based on an exact zero-order hold (ZOH) equivalent discrete SPMSM model is proposed [14], [19], but this current controller cannot be applied in salient machines. With regard to overcoming this issue, a digital current controller based on flux model is proposed [20].

For the sake of enhancing the disturbance rejection of digital current controllers, several digital current controllers have been designed. A two-degree-of-freedom digital PI current controller based on ZOH equivalent discrete model is proposed [21], but the algorithm calculation is relatively high due to the involvement of multiple deigned coefficients. Yepes *et al.* [22] have developed an optimized settling time and overshoot digital current controller with ARTF where the dynamic response and disturbance rejection coefficients are theoretically designed. In order to analyze the computation and modulation delay effect on ARTF, a second-order Pade expansion was employed and it has been found that the delay can negatively affect the pole-zero cancelation. In addition, they proposed a digital current controller by adding an active inductance term feedback to enhance the disturbance rejection, but the dominant poles are closer to the stability boundary [23]. To reduce the ARTF delay effect on digital current controllers, Vukosavic *et al.* [24] designed a digital current controller with an error-free sampling and ARTF. In this structure, the current controller is modified by adding a delay model $z^{-1.5T_s}$, which can further improve current dynamic response by extending the range of permissible value of ARTF. Another method to suppress ARTF delay model is employing a prediction scheme [18]. In this prediction scheme, the next instant stator current can be obtained based on a machine model and can directly compensate the ARTF delay, but this scheme strongly depends on the machine model accuracy.

Based on the ARTF structure, with regard to pursuing the high performance of digital current controllers including the dynamic response, disturbance rejection, and parameter robustness, it is indispensable to design a digital current controller considering the computation and modulation delay. However, few effective approaches are developed except for several references [18], [22], [24]. Motivated by this fact, this article proposes a digital current controller with ARTF by employing a digital internal mode control (IMC) current estimator. The contributions of this article are as follows.

1) A digital IMC current estimator based on the exact ZOH equivalent discrete SPMSM with ARTF model is proposed. In this proposed structure, the superposition principle is employed and relatively low parameter sensitivity (considering SPMSM parameter disturbances) will occur compared with the current prediction scheme [18]. The predicted current can be effectively utilized as the ARTF delay compensation. Moreover, the predicted current can be directly regarded as the feedback of current controller to suppress the execution time delay effect on the overall system. Based on the proposed current estimator, an improved digital current controller considering the execution and modulation delay is proposed, where the dynamic response, disturbance rejection, and parameter robustness can be enhanced.

2) Considering the ARTF and current loop feedback disturbance paths effect on the overall control system, the designed coefficients, dynamic response, disturbance rejection, and parameter robustness based on the exact ZOH equivalent discrete SPMSM model are theoretically illustrated in detail. In order to illustrate the superiority of the proposed digital current controller with ARTF, two state-of-the-art digital current controllers with ARTF will be compared.

The rest of this article is organized as follows. Section II introduces the exact ZOH equivalent discrete dq-axis SPMSM model and state-of-the-art digital current controllers with ARTF. The proposed digital current controller with ARTF is presented in Section III. In order to make a detailed theoretical analysis of current controller performance, the performance evaluation of the proposed digital controller with ARTF compared with two state-of-the-art digital current controllers with ARTF is presented in Section IV. Experimental verification of four digital current controllers is carried out in Section V. Finally, Section VI concludes this article.

II. Exact ZOH Equivalent Discrete SPMSM Model and Digital Current Controller With ARTF Design

In this section, the exact ZOH equivalent discrete dq-axis SPMSM model is introduced. Based on the discrete model, two types of state-of-the-art digital current controllers with ARTF are presented.

A. Exact ZOH Equivalent Discrete DQ-Axis SPMSM Model

The $\alpha\beta$-axis SPMSM voltage and stator flux linkage equations considering inverter nonlinearity [25], [26] are shown in $\alpha\beta$

$$\begin{cases} U_s^{\text{ref}} = R_s i_s + \dot{\psi}_s + U_s' \\ \psi_s = L_s i_s + \psi_m e^{j\theta_e} \end{cases} \tag{1}$$

where the superscript "$\cdot$" means the derivative with respect to time. To get the discretization of SPMSM model based on (1), the differential equation needs to be solved. The brief procedure can be presented as follows. First, U_s' and $\psi_m\omega_e$ are considered as disturbance terms and the current vectors i_s in continuous-time domain can be obtained as

$$i_s(t) = e^{-\frac{R_s}{L_s}t} i_s(t_0) + \left(1 - e^{-\frac{R_s}{L_s}t}\right) \frac{1}{R_s} U_s(t) \tag{2}$$

where $i_s(t_0)$ means the initial current state variables; U_s is the $\alpha\beta$-axis SPMSM stator voltage after adding the disturbance terms U_s' and $\psi_m\omega_e$.

The symmetrical pulsewidth modulation with sampling at the start of each carrier period is employed [19], as shown in Fig. 1. Apart from that, approximate $0.5T_s$ time belongs to the modulation time delay from $\alpha\beta$-axis to dq-axis. Overall, the execution and modulation time delay in digital control system can be approximately equal to $1.5T_s$[17], [22], and the dq-axis

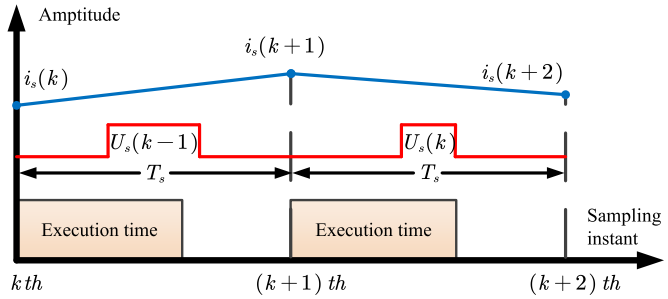

Fig. 1. Diagram of the execution delay in digital control system.

stator voltage U_{dq1} after adding the disturbance terms can be obtained as

$$U_s(t-T_s) = e^{j\theta_e}\frac{1}{T_s}\int_{T_s}^{2T_s} U_{dq1}(t-\tau)e^{-j\omega_e\tau}d\tau \approx e^{-j\omega_e 1.5T_s}e^{j\theta_e}U_{dq1}(t-1.5T_s). \tag{3}$$

Based on (2) and (3), the discrete-time dq-axis current i_{dq} based on ZOH model can be presented as [17], [22]

$$i_{dq}(k+1)e^{j\omega_e T_s} = i_{dq}(k)e^{-\frac{R_s T_s}{L_s}} + \left(1-e^{-\frac{R_s}{L_s}T_s}\right)\frac{1}{R_s}\overbrace{e^{-j\omega_e 1.5T_s}U_{dq1}(k-1.5)}^{1.5T_s\ \text{approximate delay}}. \tag{4}$$

The transfer function $G_{p0}(z)$ of the exact ZOH equivalent discrete SPMSM model can be expressed as follows:

$$G_{p0}(z) = \frac{i_{dq}(z)}{U_{dq1}(z)} = \frac{1-e^{-\frac{R_s}{L_s}T_s}}{R_s\overbrace{e^{j\omega_e 1.5T_s}z^{1.5}}^{1.5T_s\ \text{delay}}\left(ze^{j\omega_e T_s}-e^{-\frac{R_s}{L_s}T_s}\right)}. \tag{5}$$

B. Digital Current Controller With ARTF

Regarding adding ARTF in digital current controllers, it can be known that the disturbance rejection of current controllers is improved by moving the plant pole location [22], [27]. In this section, the two previous digital current controllers with ARTF are illustrated herein, namely digital current controller with ARTF by prediction scheme [18] and IMC digital current controller with ARTF [22], [24]. In order to reduce the calculation, the term $e^{-\frac{R_s}{L_s}T_s}$ can be simplified as the term $1-\frac{R_s}{L_s}T_s$ (see, e.g., [24, Fig. 1]). The disturbance terms U_s' and $\psi_m\omega_e$ of plant are assumed to be fully eliminated by the feedforward terms. To compensate the electrical angle θ_e delay caused by the execution and modulation time delay, the modified park transform coefficient K can be designed as $e^{j\omega_e 1.5T_s}$.

1) Digital Current Controller With ARTF by Prediction Scheme: Since the modulation and control delay prevents the pole-zero cancelation between the plant and controller (see, e.g., [22, (16)]), the current prediction scheme will be employed herein. Based on the accurate SPMSMs model [18], the next instant predicted current $\widehat{i_{dq}}$ can be obtained as

$$z\widehat{i_{dq}}(z) = i_{dq}(z) + \frac{T_s}{L}[z^{-1}U_{dq}^{ref}(z) - z^{-1}U_{dq}'(z) - Ri_{dq}(z) - jL\omega_e i_{dq}(z) - j\psi\omega_e]. \tag{6}$$

$G_{p0}(z)$ with ARTF can be simplified to $G_{p1}(z)$, which is shown as follows:

$$G_{p1}(z) = \frac{\frac{T_s}{L_s}}{z^{1.5}\left[ze^{j\omega_e T_s}-(1-\frac{R_s+z^{-0.5}R_v}{L_s}T_s)\right]} \tag{7}$$

where R_v means the ARTF gain. In order to establish the digital current controller with ARTF, the value of actual SPMSM parameters is assumed to be equal to the value of the parameters in controller, i.e., $L_s = L, \psi_m = \psi, R_s = R$, and, hence, the transfer function $G_{c1}(z)$ of the current controller with ARTF is presented as [22]

$$G_{c1}(z) = \alpha_1\frac{L}{T_s}\left[e^{j\omega_e T_s}-\left(1-\frac{R+R_v}{L}T_s\right)z^{-1}\right]\frac{z}{z-1} \tag{8}$$

where α_1 denotes the angular frequency of the controller.

2) Digital IMC Current Controller With ARTF: Another alternative is a digital IMC current controller by adding a delay model. Considering the inherent delay model $z^{-1.5T_s}$, $G_{p0}(z)$ with ARTF can be rearranged as

$$G_{p2}(z) = \frac{\frac{T_s}{L_s}}{z^{1.5}\left[ze^{j\omega_e T_s}-(1-\frac{R_s+z^{-1.5}R_v}{L_s}T_s)\right]}. \tag{9}$$

To make a perfect pole-zero cancelation, the inherent delay model $z^{-1.5T_s}$ needs to be added into the digital current controller with ARTF [22], [24]. Based on IMC principle, $G_{c2}(z)$ can be equal to $G_{p2}^{-1}(z)l(z)d(z)$, where $d(z)$ is an adjustable model based on a plant. In order to build the first-order closed-loop current system transfer function, a discrete-time integrator $l(z)$ can be expressed as $\frac{z\alpha_1}{z-1}$. To make a causal system in the current controller, the adjustable model $d(z)$ needs to be designed as $\frac{1}{z^{2.5}}$. Compared with the digital current controller with ARTF by prediction scheme, the dynamic response performance of this current controller is enhanced due to better pole-zero cancelation. The current controller model $G_{c2}(z)$ can be obtained as [22]

$$G_{c2}(z) = \alpha_1\frac{L}{T_s}\left[e^{j\omega_e T_s}-\left(1-\frac{R+z^{-1.5}R_v}{L}T_s\right)z^{-1}\right]\frac{z}{z-1}. \tag{10}$$

The block diagrams of the two digital current controllers are shown in Fig. 2.

III. Proposed Digital Current Controller

Compared with the above two digital current controllers with ARTF, this article proposes an improved digital current controller with ARTF by employing a digital IMC current estimator, where the dynamic response, disturbance rejection, and parameter robustness are enhanced. The proposed digital current

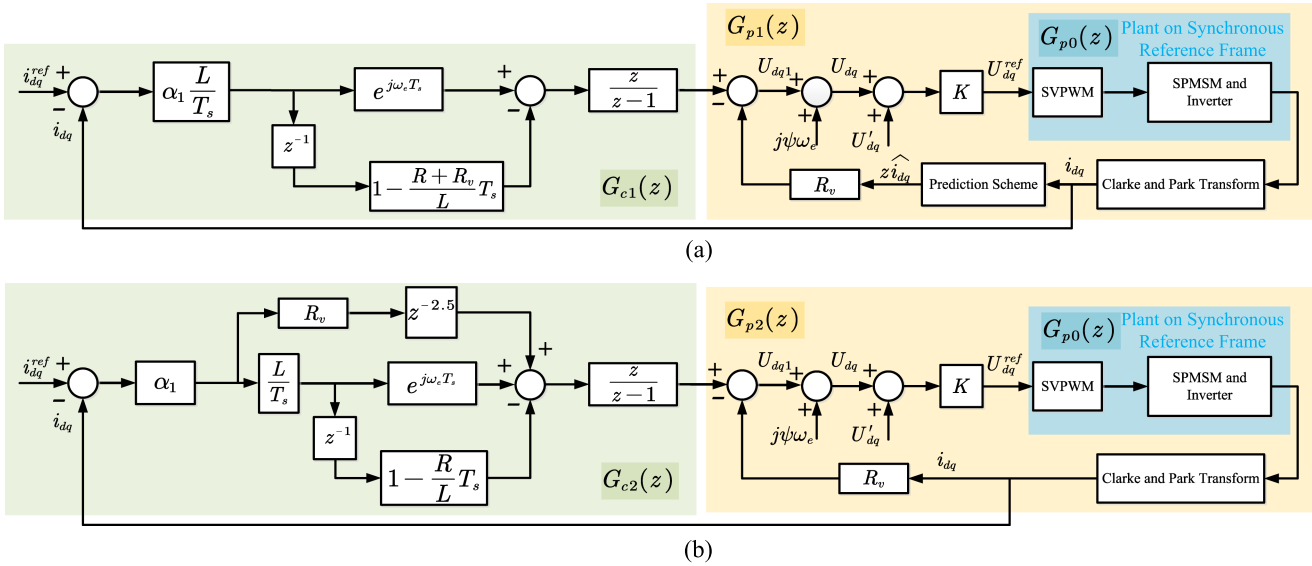

Fig. 2. Block diagram of overall control loops for the two digital current controllers with ARTF. (a) Digital current controller with ARTF by prediction scheme. (b) IMC digital current controller with ARTF.

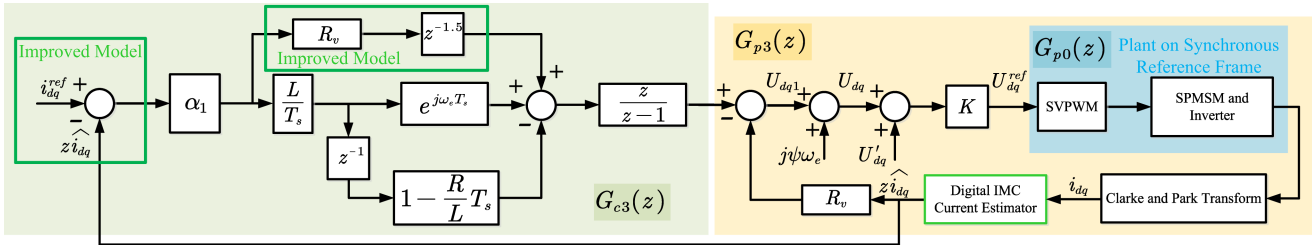

Fig. 3. Block diagram of the overall control loop for the proposed digital current controllers with ARTF.

controller and digital IMC current estimator will be illustrated in this section.

A. Improved Digital Current Controller With ARTF

Motivated by the prediction scheme based on (6), a digital IMC current estimator is proposed. In the proposed digital IMC current estimator structure, the next instant current $z\widehat{i_{dq}}$ can be obtained with low parameter sensitivity compared with the prediction scheme based on (6) and $z\widehat{i_{dq}}$ can suppress the ARTF delay issue. Moreover, $z\widehat{i_{dq}}$ can be considered as the feedback of current controller, which can improve the overall system performance, as illustrated in the next section in detail. In addition, a delay model $z^{-0.5T_s}$ is added in the current controller to compensate the modulation delay from dq-axis to $\alpha\beta$-axis. Therefore, the modified plant model $G_{p3}(z)$ can be expressed as

$$G_{p3}(z)=\frac{\frac{T_s}{L_s}}{z^{1.5}\left[ze^{j\omega_e T_s}-\left(1-\frac{R_s+z^{-0.5}R_v}{L_s}T_s\right)\right]}. \tag{11}$$

Based on the pole-zero cancelation, the proposed controller model $G_{c3}(z)$ can be expressed as

$$G_{c3}(z)=\alpha_1\frac{L}{T_s}\left[e^{j\omega_e T_s}-\left(1-\frac{R+z^{-0.5}R_v}{L}T_s\right)z^{-1}\right]\frac{z}{z-1}. \tag{12}$$

The block diagram of the proposed overall control loop is shown in Fig. 3. The digital implementation of the improved digital current controller can be presented as

$$\begin{cases} e_{dq1}(k)=i_{dq}^{ref}(k)-\widehat{i_{dq}}(k+1) \\ U_{dq2}(k)=R_v\alpha_1 e_{dq1}(k-1.5) \\ U_{dq3}(k)=e_{dq1}(k)\alpha_1 e^{j\omega_e T_s}\frac{L}{T_s} \\ U_{dq4}(k)=e_{dq1}(k-1)\alpha_1\frac{L}{T_s}(1-\frac{RT_s}{L}) \\ U_{dq5}(k)=-U_{dq2}(k)+U_{dq3}(k)+U_{dq4}(k) \\ U_{dq6}(k)=U_{dq5}(k)+U_{dq6}(k-1) \\ U_{dq1}(k)=U_{dq6}(k)-\widehat{i_{dq}}(k+1)R_v. \end{cases} \tag{13}$$

The optimum value of R_v can be equal to the proportional gain of the current controller [24]. In this case, R_v can be expressed as

$$R_v=\frac{\alpha_1 L}{T_s}. \tag{14}$$

It should be noted that R_v is related to disturbance rejection and the optimum value of R_v is only based on the value of α_1 without parameter mismatch [22]. The value of R_v needs to be adjusted under different parameter mismatch conditions, i.e., $L \neq L_s$. If the machine speed over sampling frequency of the system is relatively small, $e^{j\omega_e T_s} \approx 1 + j\omega_e T_s$ can be satisfied in (13), where the calculation can be further reduced. Overall, the proposed digital current controller can be utilized under different conditions.

B. Digital IMC Current Estimator

In order to design the digital IMC current estimator, $z^{-1}U_{dqf}(z)$, $z\widehat{i_{dq}}(z)$, and $z^{-1}U_{dq0}(z)$ are taken as input, output variables, and disturbances of the plant, respectively. Equation (11) can be considered as the plant in the proposed IMC current estimator since ARTF is added in the control system. $z^{-1}U_{dq0}(z)$ can be acquired at the kth instant as

$$z^{-1}U_{dq0}(z) = z^{-1}\frac{U_{dq}^{\text{ref}}(z)}{K} - z^{-1}U'_{dq}(z) - j\psi\omega_e + \widehat{i_{dq}}(z)R_v \tag{15}$$

where U_{dqf} denotes the disturbance voltage caused by SPMSM parameter mismatch. It should be noted that different from the prediction scheme of (6) which does not consider the disturbances U_{dqf} caused by parameter mismatch, U_{dqf} can be acquired in the proposed digital IMC current estimator. Based on $G_{c3}(z)$, the SPMSM with ARTF plant $G_{pf}(z)$ of the estimator can be built as

$$G_{pf}(z) = \frac{z\widehat{i_{dq}}}{z^{-1}U_{dqf}(z)} = \frac{\frac{T_s}{L}}{z^{0.5}\left[e^{j\omega_e T_s} - (1 - \frac{R+z^{-0.5}R_v}{L}T_s)z^{-1}\right]}. \tag{16}$$

Based on IMC principle, the feedforward path model of the IMC current estimator $G_{fc}(z)$ can be presented as $G_{fc}(z) = \frac{z}{z-1}\alpha_2$, where α_2 is the desired angular frequency of the estimator. Employing the superposition principle, i.e., the sum of feedforward and disturbance paths, the output $z\widehat{i_{dq}}(z)$ of plant can be easily acquired as

$$\begin{aligned} z\widehat{i_{dq}}(z) &= i_{dq}(z)\overbrace{\frac{G_{fc}(z)}{1+z^{-1}G_{fc}(z)}}^{\text{Term1}} \\ &\quad + z^{-1}U_{dq0}(z)\overbrace{\frac{G_{pf}(z)}{1+z^{-1}G_{fc}(z)}}^{\text{Term2}} \\ &= \overbrace{i_{dq}(z)}^{\text{Measurement}} + \overbrace{\frac{z^{-1}U_{dq0}(z)G_{pf}(z)(z-1)+i_{dq}(z)b_1}{z-1+\alpha_2}}^{\text{Prediction}} \end{aligned} \tag{17}$$

where $b_1 = \alpha_2 z - z + 1 - \alpha_2$. The block diagram of the digital IMC current estimator is shown in Fig. 4. In (17), it is noticeable

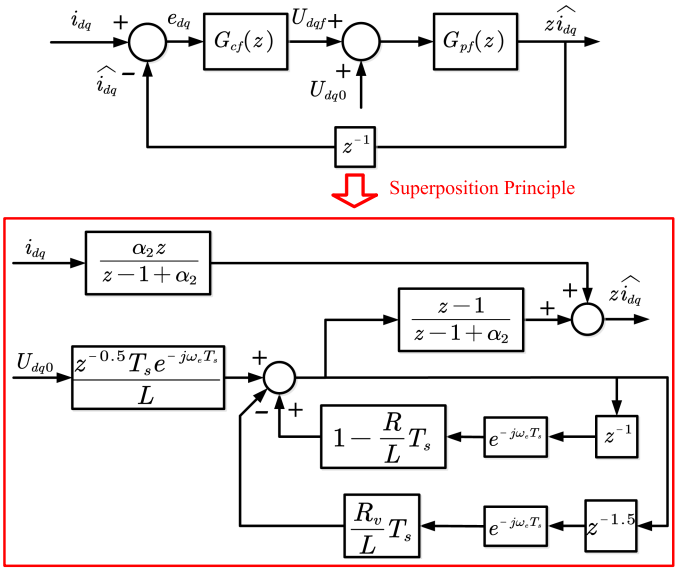

Fig. 4. Block diagram of digital IMC current estimator based on superposition principle.

that the dynamic response of the IMC current estimator is determined by Term1 and Term2 both. Apart from that, it can be seen that Term1 is a first-order low-pass filter, and, hence, the value of α_2 can be set as $\alpha_2 \in (0, 1]$ according to the pole-zero location of the transfer function. In addition, the other format of (17) can show the instantaneous predicted current characteristic, and it can include two parts, i.e., measurement and prediction parts. The measurement part can reduce parameter sensitivity, while the prediction part can predict the next instant current.

To analyze the steady-state error of the proposed IMC current estimator, the transfer function of steady state error $e_{dq}(z)$ can be shown in (18) based on (17)

$$\begin{aligned} \lim_{t\to\infty} e_{dq}(t) &= \lim_{z\to 1}(z-1)e_{dq}(z) \\ &= \lim_{z\to 1}\left[i_{dq}(z)\frac{z-1}{1+z^{-1}G_{fc}(z)} \right. \\ &\quad \left. + z^{-1}U_{dq0}(z)\frac{-(z-1)G_{pf}(z)z^{-1}}{1+z^{-1}G_{fc}(z)}\right] = 0. \end{aligned} \tag{18}$$

It can be seen that the value of the steady error can keep zero with parameter mismatch, which means that $i_{dq}(t) = \widehat{i_{dq}}(t)$. From the transfer function of steady-state error, it can be known that the parameter mismatch can affect the estimated current dynamic response and then the overall system will be influenced. The overall system performance evaluation is analyzed in the next section.

After designing the digital IMC current estimator, the digital implementation of the (k+1)th instant predicted currents can be

acquired as follows:

$$\begin{cases} r_1(k) = U_{dq0}(k-1.5)\frac{T_s e^{-1.5j\omega_e T_s}}{L} \\ r_2(k) = r_1(k) + r_3(k-1)e^{-j\omega_e T_s}(1-\frac{R}{L}T_s) \\ r_3(k) = r_2(k) - r_3(k-1.5)e^{-j\omega_e T_s}\frac{R_v}{L}T_s \\ r_4(k) = r_3(k) - r_3(k-1) - r_4(k-1)(\alpha_2-1) \\ r_5(k) = i_{dq}(k)\alpha_2 - r_5(k-1)(\alpha_2-1) \\ \widehat{i_{dq}}(k+1) = r_5(k) + r_4(k). \end{cases} \tag{19}$$

IV. Performance Evaluation of the Proposed Digital Current Controller With ARTF

In order to better analyze the performance of the proposed digital current controller, the three digital current controllers with ARTF will be compared in detail. The current response performance of the three digital current controllers with ARTF will be, respectively, expressed as follows:

$$\begin{aligned} i_{dq}(z) &= G_{cl1}(z)i_{dq}^{\text{ref}}(z) + G_{\text{dis1}}(z)d_{\text{dis}}(z) \\ i_{dq}(z) &= G_{cl2}(z)i_{dq}^{\text{ref}}(z) + G_{\text{dis2}}(z)d_{\text{dis}}(z) \\ i_{dq}(z) &= G_{cl3}(z)i_{dq}^{\text{ref}}(z) + G_{\text{dis3}}(z)d_{\text{dis}}(z) \end{aligned} \tag{20}$$

where $G_{cl1}(z), G_{cl2}(z),$ and $G_{cl3}(z)$ denote the three current controllers closed-loop transfer functions, respectively; d_{dis} stands for the disturbances caused by parameter mismatch including ψ, R, $jL\omega_e i_{dq}$, $\frac{R+R_v}{L}$, $\frac{R+z^{-0.5}R_v}{L}$, and $\frac{R+z^{-1.5}R_v}{L}$[1]; $G_{\text{dis1}}(z), G_{\text{dis3}}(z),$ and $G_{\text{dis3}}(z)$ mean the three current controllers disturbance transfer functions, respectively. Since d_{dis} can be taken as disturbances caused by stator inductance, stator resistance, and rotor flux linkage parameter mismatch, the analysis of disturbance transfer functions can reflect the performance impact of the parameter mismatch controller on the system. In digital current controllers with ARTF, the digital current controller with prediction scheme [18], the IMC digital current controller [22], [24], and proposed digital current controller are named after Method1, Method2, and Method3, respectively. The block diagram of the three current controllers considering disturbance paths are shown in Fig. 5. It can be seen that the current loop feedforward disturbance d_{dis} caused by controller parameter mismatch exists in the three methods. In addition, Method1 and Method3 contain an ARTF disturbance path, while the current loop feedback disturbance paths exists in Method3. Because the disturbances d_{dis} are all caused by the SPMSM parameter mismatch, d_{dis} can be approximately assumed as the same value in the different disturbance paths.

A. Dynamic Response Performance Evaluation

In order to evaluate the current dynamic response performance of the proposed digital current controller, parameter mismatch is not considered herein. The three current closed-loop transfer

[1]Apart from the term $jL\omega_e i_{dq}$, $\frac{R+R_v}{L}$, $\frac{R+z^{-0.5}R_v}{L}$, $\frac{R+z^{-1.5}R_v}{L}$, the term $\frac{T_s}{L}$ under parameter mismatch cannot be taken as d_{dis} (e.g., see [11]). The term $\frac{T_s}{L}$ parameter mismatch effect on the overall system will be analyzed in the next section.

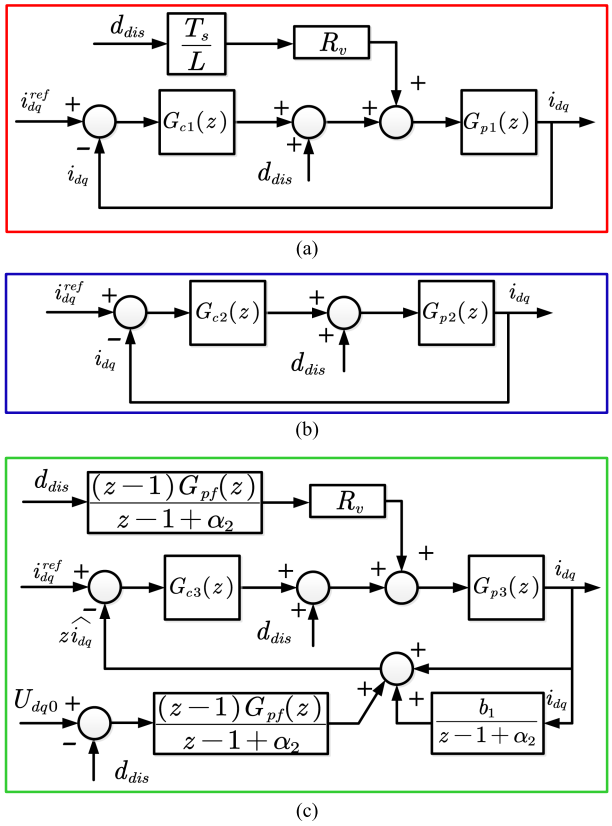

Fig. 5. Block diagram of the three current controllers considering disturbance paths. (a) Digital current controller with ARTF by prediction scheme. (b) IMC digital current controller with ARTF. (c) Proposed digital current controller with ARTF.

functions $G_{cl1}(z), G_{cl2}(z),$ and $G_{cl3}(z)$ can be presented as

$$\begin{aligned} G_{cl1}(z) &= \frac{G_{p1}(z)G_{c1}(z)}{1+G_{p1}(z)G_{c1}(z)} = \frac{G_d(z)}{z^{2.5}-z^{1.5}+G_d(z)} \\ G_{cl2}(z) &= \frac{G_{p2}(z)G_{c2}(z)}{1+G_{p2}(z)G_{c2}(z)} = \frac{\alpha_1}{z^{2.5}-z^{1.5}+\alpha_1} \\ G_{cl3}(z) &= \frac{G_{p3}(z)G_{c3}(z)}{1+G_{p3}(z)G_{c3}(z)} = \frac{\alpha_1}{z^{2.5}-z^{1.5}+\alpha_1 z} \end{aligned} \tag{21}$$

where $G_d(z)$ can be expressed as $G_d(z) = \alpha_1 \frac{e^{j\omega_e T_s}-(1-\frac{R+R_v}{L}T_s)}{e^{j\omega_e T_s}-(1-\frac{R+R_v z^{-0.5}}{L}T_s)}$. Based on the above term, it can be known that the ARTF delay prevents the pole-zero cancelation in $G_{cl1}(z)$, where Yepes *et al.* have analyzed that the imperfect pole-zero cancelation can negatively affect the current controller performance (see, e.g., [22, (16)]). In addition, since it is not straightforward to analyze the decimal format models in z domain, the half delay $z^{-0.5}$ will be neglected to simplify the analysis in this article. Thus, the three transfer functions can become the second-order system and $G_{cl1}(z)$ is the same with $G_{cl2}(z)$. It can be easily seen that the bandwidth of G_{cl3} is not the same with G_{cl1} and G_{cl2} under the same value of α_1 due to different transfer function models. The poles of G_{cl1} and G_{cl2} are $\frac{1+\sqrt{1-4\alpha_1}}{2}$ and $\frac{1-\sqrt{1-4\alpha_1}}{2}$, respectively. On the contrary,

the poles of G_{cl3} are 0 and $1-\alpha_1$, respectively. From the pole location, when $\alpha_1 \in \left(0, \frac{1}{4}\right]$, the system G_{cl1}, G_{cl2} is underdamped, i.e., it means the current overshoot can occur under the range value of $\alpha_1 \in \left[\frac{1}{4}, 1\right]$ in the system G_{cl1}, G_{cl2}. However, the current overshoot of G_{cl3} cannot occur under the large range value of $\alpha_1 \in (0, 1]$. In other words, it can be known that the dynamic response of Method1 and Method2 is deteriorated with the increase of α_1 compared with Method3.

In order to validate the above analysis, the three sets of respectively same current bandwidth in G_{cl1}, G_{cl2}, and G_{cl3} will be carried out in simulation, i.e., ($\alpha_1 = 0.3$ of G_{cl1}, G_{cl2} and $\alpha_1 = 0.48$ of G_{cl3}), ($\alpha_1 = 0.39$ of G_{cl1}, G_{cl2} and $\alpha_1 = 0.6$ of G_{cl3}), and ($\alpha_1 = 0.53$ of G_{cl1}, G_{cl2} and $\alpha_1 = 0.68$ of G_{cl3}). In Fig. 6, it can be seen that the dynamic response performance under low current bandwidth is almost the same in Fig. 6(a). However, there exists positive magnitude in the Bode plot of G_{cl1}, G_{cl2} in Fig. 6(b) and (c), which means that the current overshoot can occur under the step current response. In addition, when the value of α_1 increases, the positive magnitude goes larger. In this article, the maximum value of current overshoot is limited to 150% reference current, which means that the maximum magnitude of $G_{cl1}, G_{cl2},$ and G_{cl3} is 3.52 dB as shown in Fig. 6(c). The simulation can effectively validate the proposed current controller and can obtain the same current dynamic response speed without overshoot compared with Method1 and Method2.

B. Disturbance Rejection Evaluation

The disturbance transfer functions from d_{dis} to the current variation Δi_{dq} caused by the disturbances in the three methods are respectively shown in the following equation:

$$\begin{aligned}
G_{\text{dis1}}(z) &= \frac{\Delta i_{dq}(z)}{d_{\text{dis}}(z)} \\
&= \left(1 + R_v \frac{T_s}{L}\right) G_{p1}(z) \frac{z^{2.5} - z^{1.5}}{z^{2.5} - z^{1.5} + G_d(z)} \\
G_{\text{dis2}}(z) &= \frac{\Delta i_{dq}(z)}{d_{\text{dis}}(z)} = G_{p2}(z) \frac{z^{2.5} - z^{1.5}}{z^{2.5} - z^{1.5} + \alpha_1} \\
G_{\text{dis3}}(z) &= \frac{\Delta i_{dq}(z)}{d_{\text{dis}}(z)} = \left[G_{p3}(z) + G_r(z)\right] \frac{z^{2.5} - z^{1.5}}{z^{2.5} - z^{1.5} + \alpha_1 z} \\
G_r(z) &= \left[\frac{\alpha_1}{z^{2.5} - z^{1.5}} + R_v G_{p3}(z)\right] \frac{(z-1) G_{pf}(z)}{z - 1 + \alpha_2}.
\end{aligned} \tag{22}$$

An effective disturbance rejection evaluation is to employ a magnitude form integrated error [22], but it is complicated to obtain the explicit solution due to the involvement of the plant complex vector. In order to simplify the model, the cross-coupling term is not considered. Therefore, the integrated error ζ can be presented in (23), where a unit disturbance step $d_{\text{dis}}(z) = \frac{z}{z-1}$ and final value theorem z transform are applied herein

$$\begin{aligned}
\zeta &= \int_0^\infty \Delta i_{dq} d\tau = \int_0^\infty G_{\text{dis}}(z) d_{\text{dis}}(z) d\tau \\
&= \lim_{z \to 1} z G_{\text{dis}}(z) d_{\text{dis}}(z).
\end{aligned} \tag{23}$$

The integrated error of the three methods $\zeta_1, \zeta_2,$ and ζ_3 can be solved by (22) and (23) as follows:

$$\begin{aligned}
\zeta_1 &\approx \left(1 + \frac{R_v T_s}{L}\right) \frac{1}{\alpha_1 (R_s + R_v)} = \frac{1}{\alpha_1 R_s + \frac{\alpha_1^{2\tilde{}} L}{T_s}} \\
&\quad + \overbrace{\frac{1}{R_s + \frac{\alpha_1 L}{T_s}}}^{\text{Term3}} \\
\zeta_2 &\approx \frac{1}{\alpha_1 (R_s + R_v)} = \frac{1}{\alpha_1 R_s + \frac{\alpha_1^2 L}{T_s}} \\
\zeta_3 &\approx \left[1 + \frac{\alpha_1}{\alpha_2 (R + R_v)}\right] \frac{1}{\alpha_1 (R_s + R_v)} \\
&\approx \frac{1}{\alpha_1 R_s + \frac{\alpha_1^2 L}{T_s}} + \overbrace{\frac{1}{\alpha_2 (R + \frac{\alpha_1 L}{T_s})(R_s + \frac{\alpha_1 L}{T_s})}}^{\text{Term4}}.
\end{aligned} \tag{24}$$

From (24), it can be easily seen that the disturbance rejection is enhanced (the values of $\zeta_1, \zeta_2,$ and ζ_3 become small) with the values of R_s, R, α_1, and α_2 increasing in the current controllers with ARTF. Due to adding Term3 in ζ_1, $\zeta_1 > \zeta_2$, which means that Method2 has better disturbance rejection than Method1. Although Term4 exists in ζ_3, α_1 of Method3 is larger than α_1 of Method1 and Method2 to keep the same dynamic response. It is complicated to compare the values between ζ_2 and ζ_3 under whole conditions. Employing the machine parameter of this article, setting α_2 as 1, ζ_3 can keep the lowest value based on the numerical solution under several different values of α_1. In terms of external disturbance rejection, i.e., the disturbance caused by $j\psi\omega_e$ in the current loop feedforward path, it can be seen that Term3 and Term4 are removed from (24). The best external disturbance rejection is in Method3 due to larger value of α_1. Overall, with the same current dynamic response in the three digital current controllers, the proposed digital current controller has the best disturbance rejection.

C. Parameter Robustness Performance Evaluation

In order to analyze the parameter robustness of the three methods, the three current open-loop transfer functions $\overline{G_{ol1}(z)}, \overline{G_{ol2}(z)}, \overline{G_{ol3}(z)}$ under inductance parameter mismatch ($\frac{T_s}{L} \neq \frac{T_s}{L_s}$) can be presented as

$$\begin{aligned}
\overline{G_{ol1}(z)} &= G_{p1}(z) G_{c1}(z) = \frac{\overline{G_d(z)}}{z^{2.5} - z^{1.5}} \\
\overline{G_{ol2}(z)} &= G_{p2}(z) G_{c2}(z) = \frac{\frac{\alpha_1 L}{L_s}}{z^{2.5} - z^{1.5}} \\
\overline{G_{ol3}(z)} &= G_{p3}(z) G_{c3}(z) = \frac{\frac{\alpha_1 L}{L_s}}{z^{1.5} - z^{0.5}}
\end{aligned} \tag{25}$$

where $\overline{G_d(z)}$ can be expressed as $\overline{G_d(z)} = \frac{\alpha_1 L}{L_s} \frac{e^{j\omega_e T_s} - (1 - \frac{R + R_v}{L} T_s)}{e^{j\omega_e T_s} - (1 - \frac{R + R_v z^{-0.5}}{L} T_s)}$. Similarly, the half delay $z^{-0.5}$ will be neglected to simplify the model. The vector margin (ν_m) is employed to reflect the robustness or relative stability of

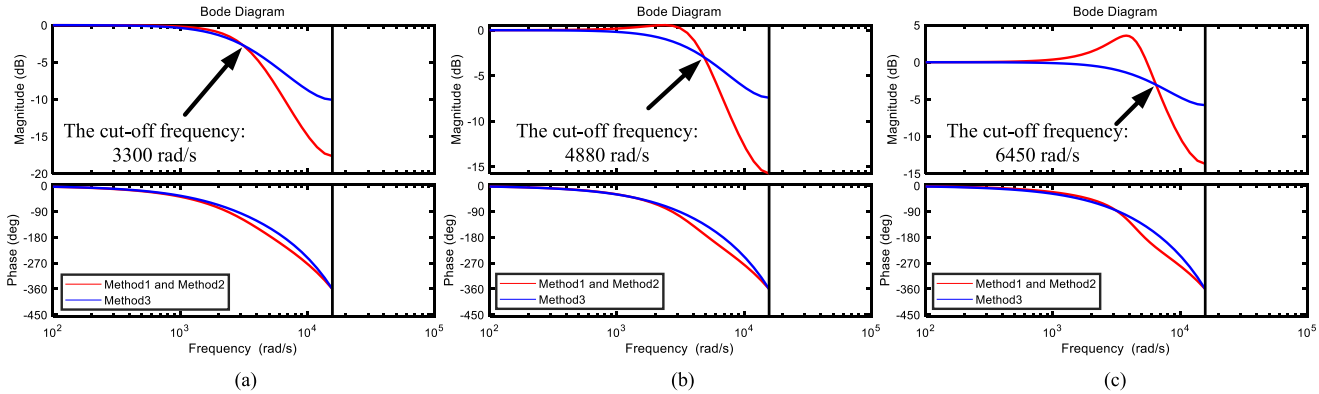

Fig. 6. Bode plot of dynamic response in the three methods. (a) Small value of current bandwidth ($\alpha_1 = 0.3$ of G_{cl1}, G_{cl2} and $\alpha_1 = 0.48$ of G_{cl3}). (b) Larger value of current bandwidth ($\alpha_1 = 0.39$ of G_{cl1}, G_{cl2} and $\alpha_1 = 0.6$ of G_{cl3}). (c) Largest value of current bandwidth ($\alpha_1 = 0.53$ of G_{cl1}, G_{cl2} and $\alpha_1 = 0.68$ of G_{cl3}).

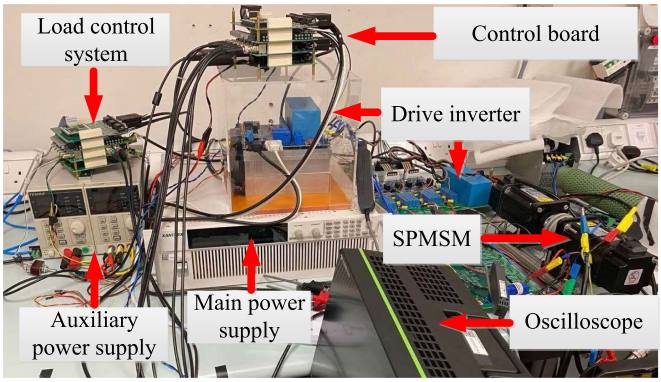

Fig. 7. Test rig of SPMSM drive system.

the closed-loop system [14]. The values of ν_m lower than 0.5 are usually associated with elevated sensitivity to parameter mismatch and with oscillatory response. Based on (25), it should be known that ν_m is reduced with the increase of $\frac{\alpha_1 L}{L_s}$, and the digital current controller with small value of α_1 can have strong parameter robustness. First, the small value of current bandwidth in the three methods is applied, i.e., $\alpha_1 = 0.3$ of G_{cl1}, G_{cl2} and $\alpha_1 = 0.48$ of G_{cl3}. When $L \leq 2.2L_s$ in Method1 and Method2, and $L \leq 3.6L_s$ in Method3, $\nu_m \geq 0.5$. After that the larger value of current bandwidth ($\alpha_1 = 0.39$ of G_{cl1}, G_{cl2} and $\alpha_1 = 0.6$ of G_{cl3}) is set in the three methods. When $L \leq 1.9L_s$ in Method1 and Method2, and $L \leq 2.9L_s$ in Method3, $\nu_m \geq 0.5$. In addition, the local stability of the proposed IMC current estimator under the inductance parameter mismatch is analyzed. The open-loop transfer function $\overline{G_{\text{olf}}(z)}$ in the proposed IMC current estimator can be expressed as $\overline{G_{\text{olf}}(z)} = \frac{\alpha_2}{z-1}$. It can be seen that the value of ν_m can keep 1 no matter how the SPMSM parameters mismatch. Overall, the proposed digital current controller has the best parameter robustness compared with Method1 and Method2. $\frac{T_s}{L}$ parameter mismatch can also affect the optimum value of R_v in Method1 and Method3 based on (14), and, hence, the disturbance rejection of overall system can be affected. For example, when $\frac{L_s}{L} > 1$, the disturbance rejection will be reduced. On the contrary, the disturbance rejection will be further enhanced with $\frac{L_s}{L} < 1$. In this case, the value of R_v should be adjusted with the magnitude of $\frac{T_s}{L}$ parameter mismatch.

In terms of α_1 and α_2 selection in practical use, the values of α_1 and α_2 can be set larger to enhance the dynamic response and disturbance rejection. However, the larger values of α_1 and α_2 can induce larger magnitude of measurement noises and overall system stability is reduced with the increase of α_1. Therefore, there is a tradeoff for α_1 and α_2 selection.

V. Experimental Verification

In order to verify the correctness of the proposed method, the test rig is established as shown in Fig. 7. The voltage of the auxiliary power supply is set to 12 V and the main power supply is taken as a dc bus in the SPMSM system. The control system includes a control board based on a dual core TMS320F28377 digital signal processor, silicon carbide (SiC) and integrated IGBT drive board, and sensor board. The high revolution Lecroy oscilloscope type is MDA8058HD. The SPMSM A phase current value is acquired by a high dynamic response current probe, while other values, i.e., measured SPMSM speed and dq-axis current can be obtained by a digital–analog conversion circuit. The detailed parameters of the drive SPMSM and inverter are displayed in Table I. In this section, three types of digital current controllers with ARTF are compared with the proposed method, namely the digital current controller with ARTF without delay compensation (benchmark), digital current controller with ARTF by prediction scheme (Method1) [18] in Fig. 2(a), and IMC digital current controller with ARTF (Method2) [24] in Fig. 2(b). The proposed digital current controller is named after Method3 where the value of α_2 keeps 1.

A. Dynamic Performance Evaluation

Because the dynamic performance is significant for the design of the current controller, the dynamic performance evaluation will be carried out first. In this section, the following terms

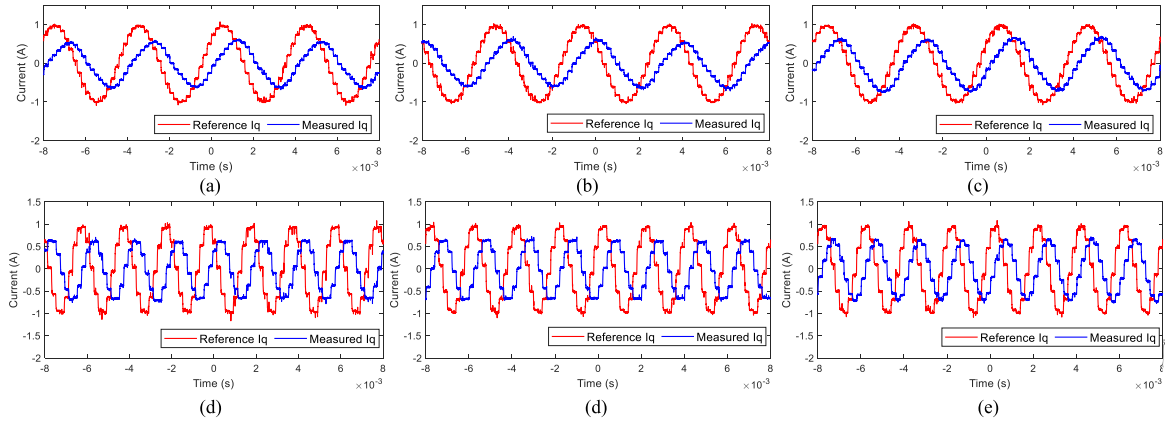

Fig. 8. Actual q-axis current performance by respectively using 250 and 500 Hz chirp signal swapping under 200 r/min speed condition. (a) and (d) Method1; (b) and (e) Method2. (c) and (f) Method3.

TABLE I
SPMSM AND INVERTER PARAMETERS

Parameters	Value	Unit
Pole pairs (p)	4	
Stator resistance (R_s)	1.1	Ω
Inverter slope resistance ($R_{ce}+R_d$)	0.02	Ω
d-axis inductance (L_d)	5.7e-3	H
q-axis inductance (L_q)	5.7e-3	H
Rotor flux linkage (ψ_m)	0.092	Wb
Rated current (I_n)	4.2	A
Rated torque (T_n)	2.3	N.m
Sampling period (T_s)	200	μs
Control period (T_s)	200	μs
Inverter deadtime (t_d)	2.5	μs

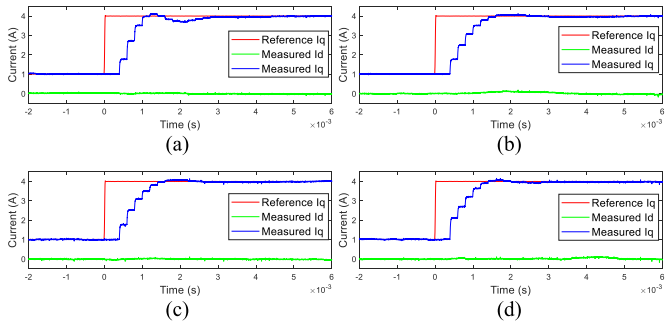

Fig. 9. dq-axis currents dynamic performance of four methods. (a) Benchmark. (b) Method1. (c) Method2. (d) Method3. (The condition: $\alpha_1 = 0.3$ in the first three methods and $\alpha_1 = 0.48$ in Method3 under 100 r/min speed condition.)

will be satisfied as: $L_s = L, \psi_m = \psi, R_s = R$, and parameter mismatch test results will be shown in Section V-C. In order to validate the simulation results of Fig. 6, the q-axis current performance by chirp signal swapping is carried out in Fig. 8. By adjusting the frequency of sinusoidal waveform, the current bandwidth α_1 can be determined when the maximum value of actual q-axis current is approximately 0.707 times of the maximum value of reference q-axis current. In this case, the 250-Hz current bandwidth can correspond to $\alpha_1 = 0.3$ in Method1 and Method2 and $\alpha_1 = 0.48$ in Method3, i.e., it is approximately consistent with the simulation results in Fig. 6(a). However, when the 500-Hz current bandwidth is set, the following test condition can be satisfied as $\alpha_1 = 0.39$ in Method1 and Method2 and $\alpha_1 = 0.68$ in Method3. It happens because the half delay $z^{-0.5}$ is neglected in the simulation, and the current bandwidth of Method1 and Method2 can vary faster than that in the simulation with the increase of α_1.

After obtaining the same current bandwidth, the dynamic response performance of the proposed current controller can be carried out. The load motor system keeps the constant value of speed and the four methods are carried out in the drive motor system. The value of the d-axis reference current is set to 0 A. In order to make the same current bandwidth in the four methods, the two sets of the same current bandwidth, i.e., $\alpha_1 = 0.3$ in the first three methods and $\alpha_1 = 0.48$ in Method3, and $\alpha_1 = 0.39$ in the first three methods and $\alpha_1 = 0.68$ in Method3 are carried out in these test results. In Fig. 9, the value of the q-axis reference current is set from 1 to 4 A and it can be seen that since ARTF delay is not compensated, the dq-axis current dynamic performance is deteriorated in benchmark. The dq-axis current dynamic performance of Method1, Method2, and Method3 almost is the same under the relatively low current bandwidth. In addition, the value of the q-axis reference current is set from 3 to 6 A. When the current bandwidth increases, i.e., $\alpha_1 = 0.39$ in the first three methods and $\alpha_1 = 0.68$ in Method3, it can be seen that the dynamic response speed becomes faster, but there exist larger current overshoot and settling time in Method1 and Method2 compared with Method3 in Fig. 10, which can validate the theoretical correctness of Fig. 6. In addition, the largest current overshoot occurs in benchmark, which can indirectly testify that the execution and modulation time delay can dramatically deteriorate the system performance.

B. External Disturbance Rejection Performance Evaluation

This type of external disturbance is established by forcing a sudden back electromotive (EMF) voltage $j\psi\omega_e$ change in the current loop feedforward path (see, e.g., [22, Figs. 15 and 16])

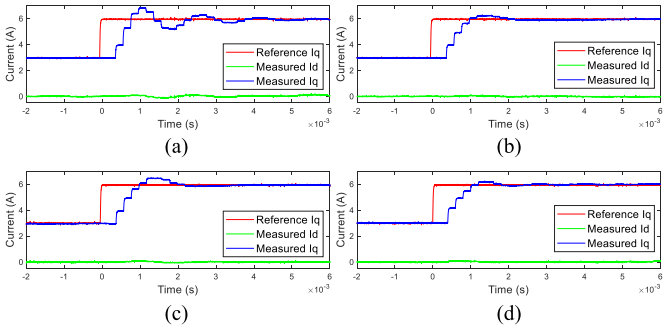

Fig. 10. dq-axis current dynamic performance of four methods. (a) Benchmark. (b) Method1. (c) Method2. (d) Method3. (The condition: $\alpha_1 = 0.39$ in the first three methods and $\alpha_1 = 0.68$ in Method3 under 100 r/min speed condition.)

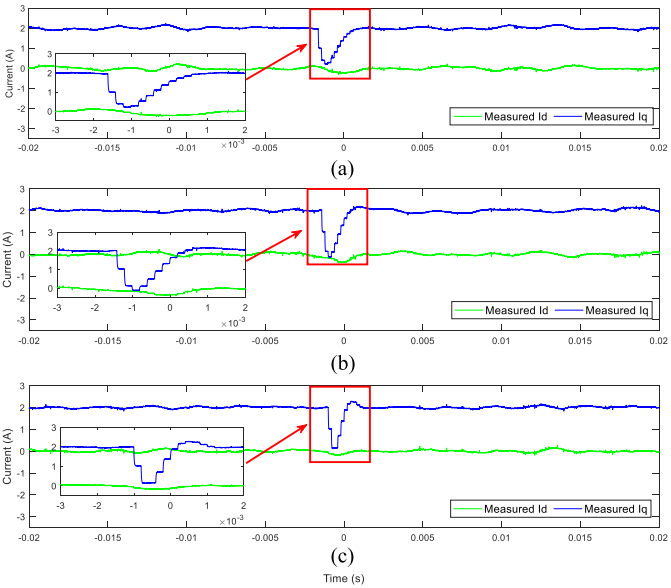

Fig. 11. External disturbance rejection performance results of three methods. (a) Method1. (b) Method2. (c) Method3. (The condition: $\alpha_1 = 0.3$ in Method1 and Method2; $\alpha_1 = 0.48$ in Method3 under 800 r/min speed condition.)

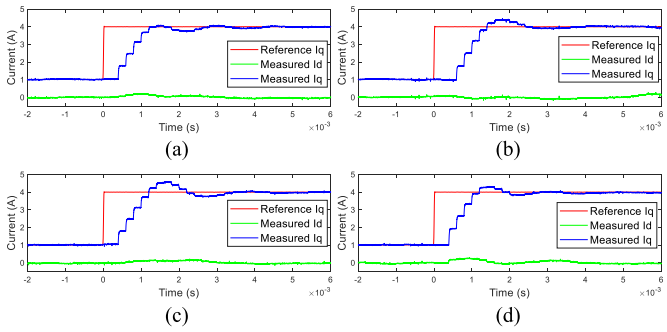

Fig. 12. dq-axis current dynamic performance of four methods under $R = 3R_s$ parameter mismatch. (a) Benchmark. (b) Method1. (c) Method2. (d) Method3.

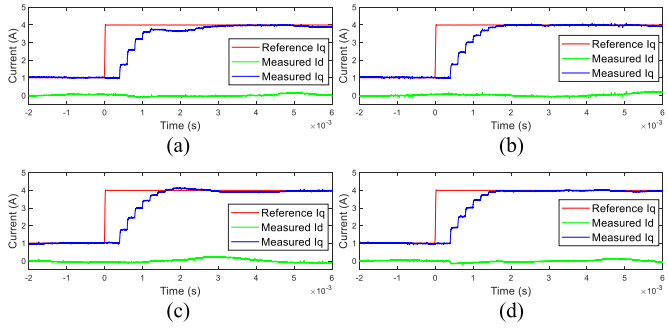

Fig. 13. dq-axis current dynamic performance of four methods under $\psi = 1.5\psi_m$ parameter mismatch. (a) Benchmark. (b) Method1. (c) Method2. (d) Method3.

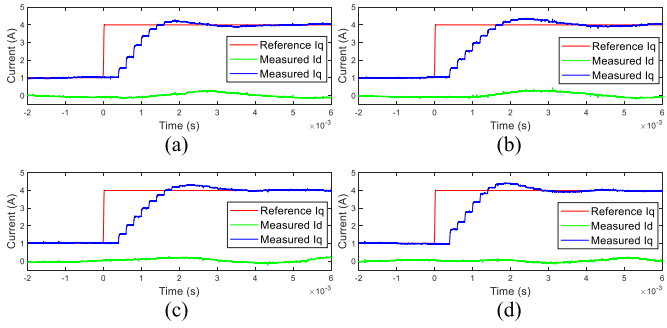

Fig. 14. dq-axis current dynamic performance of four methods under $L = 0.67L_s$ parameter mismatch. (a) Benchmark. (b) Method1. (c) Method2. (d) Method3.

while the dq-axis currents are set to 0 and 2 A, respectively, in this article. The load system keeps 800 r/min speed. It should be noted that since the sudden back EMF voltage change is only applied in the q-axis voltage equation of SPMSM, d-axis current performance can only be slightly affected due to the dq-axis coupling mechanism. In order to make a fair comparison, the same current bandwidth is set. In Fig. 11, it can be seen that the maximum value of the q-axis current overshoot is in Method2 and the minimum value of the q-axis currents settling time is in Method3. In order to evaluate the disturbance rejection performance of the proposed method, the approximate value of the integrated error ζ can be computed. Based on Fig. 11, ζ_3 is the smallest compared with ζ_1 and ζ_2, and the test results can satisfy the theoretical expectation of the disturbance rejection analysis.

C. Parameter Disturbance Performance Evaluation

In this section, the SPMSM resistance, inductance, and rotor flux linkage parameter mismatch is carried out. $\alpha_1 = 0.3$ in the first three methods and $\alpha_1 = 0.48$ in Method3 are set to keep the same current bandwidth and the SPMSM speed value is set to 400 r/min. In Fig. 12, it can be observed that the disturbance caused by resistance mismatch can dramatically affect the current dynamic response performance of digital current controllers with ARTF, and the lowest q-axis current overshoot and shortest q-axis current settling time is in Method3. When the rotor flux

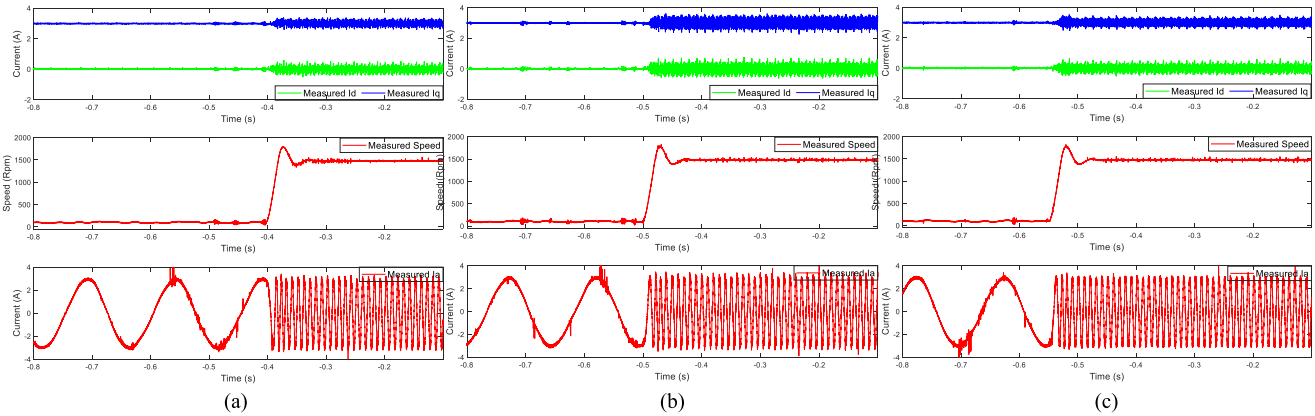

Fig. 15. dq-axis and a phase current performance of three methods from 100 to 1500 r/min motor speed. (a) Method1. (b) Method2. (c) Method3.

TABLE II
Q-AXIS CURRENT OVERSHOOT AND SETTLING TIME COMPARISON OF THE FOUR METHODS

Parameter mismatch condition	Benchmark	Method1	Method2	Method3
Settling time under $R = 3R_s$	2.8ms	2.2ms	3.2ms	1.8ms
Settling time under $R = 0.3R_s$	3ms	2.9ms	2.3ms	1.7ms
Settling time under $L = 1.5L_s$	3.8ms	3.7ms	2.8ms	1.8ms
Settling time under $L = 0.67L_s$	1.6ms	3ms	2.7ms	1.6ms
Settling time under $\psi = 1.5\psi_m$	2.2ms	1.7ms	1.65ms	1.7ms
Settling time under $\psi = 0.67\psi_m$	2.3ms	1.8ms	1.75ms	1.75ms
Overshoot under $R = 3R_s$	0.07A	0.5A	0.6A	0.26A
Overshoot under $R = 0.3R_s$	0.3A	0.8A	0.5A	0.3A
Overshoot under $L = 1.5L_s$	0A	0A	0A	0A
Overshoot under $L = 0.67L_s$	0.26A	0.42A	0.37A	0.48A
Overshoot under $\psi = 1.5\psi_m$	0A	0A	0.07A	0A
Overshoot under $\psi = 0.67\psi_m$	0A	0A	0.1A	0A

linkage parameter mismatch occurs in Fig. 13, it can be seen that the dynamic response of the four methods are almost unaffected. The reason behind this is that the speed is relatively low and the disturbance caused by the parameter mismatch $\psi = \psi_m$ is relatively small. When the parameter mismatch condition that $L = 0.67L_s$ occurs, it can be seen that the q-axis current overshoot of Method3 is larger than other methods, but the shortest settling time is in Method3, as shown in Fig. 14. In order to fully analyze the current performance under parameter mismatch in the four methods, the q-axis current overshoot and settling time comparison under different mismatch parameter conditions is listed in Table II. From this table, it can be effectively validated that Method3 is able to suppress parameter disturbances and has the best current dynamic response under parameter mismatch.

D. Steady-State Performance Under Rated Speed Condition and Current Loop Algorithm Computation Time Evaluation

To validate that the proposed digital current controller can be applied under the SPMSM rated speed condition, the steady-state current performance of the three methods under variable speed condition is presented in Fig. 15. The values of the dq-axis current are set to 0 and 3 A, respectively. It can be observed that when the motor speed is increased from the low speed 100 r/min to rated speed 1500 r/min, the magnitudes of disturbances are increased. The dq-axis maximum variation between the reference and measurement becomes larger, and Method1 and Method3 almost have the same dq-axis maximum variation, while the largest dq-axis maximum variation occurs in Method2. The total harmonic distortion of the three methods are 7.49%, 10.71%, and 7.86%, respectively. In addition, since the system clock (200 MHz) of the overall system is based on TMS320F28377 digital signal processor, the current loop algorithm computation time of the four methods is listed in Table III. From this table, it can be seen that the computation time variation between Method1 and Method3 is only 2 μs, but the current performance including dynamic response and disturbance rejection is dramatically enhanced.

TABLE III
COMPUTATION TIME OF THE FOUR METHODS

	Benchmark	Method1	Method2	Method3
Computation time	3.7μs	8.8μs	4.1μs	10.8μs

VI. CONCLUSION

In digital current controllers with ARTF structure, it is able to be experimentally applied to high performance industrial applications due to owing the simple adjustable disturbance rejection and exact ZOH equivalent discrete machine model. The theoretical analysis and experimental results have shown that the computation and execution time delay can negatively affect the current performance in terms of pursing high current bandwidth. To suppress the delay issue, an improved digital current controllers with ARTF is proposed. The experimental results have shown that the proposed digital current controller with ARTF can reduce current overshoot and settling time compared with other methods and the disturbance rejection is further enhanced since the feedback delay of current loop is compensated. Furthermore, the SPMSM parameter robustness is improved based on the vector margin analysis and test results.

The future perspective for this work can be listed as follows. An exact ZOH equivalent discrete salient ac machine model can be established and a universal digital current controller with ARTF should be developed. Advanced modulation and sampling techniques should be developed to further suppress the modulation and execution delay.

REFERENCES

[1] P. L. Jansen and R. D. Lorenz, "A physically insightful approach to the design and accuracy assessment of flux observers for field oriented induction machine drives," *IEEE Trans. Ind. Appl.*, vol. 30, no. 1, pp. 101–110, Jan./Feb. 1994.

[2] D. Casadei, F. Profumo, G. Serra, and A. Tani, "FOC and DTC: Two viable schemes for induction motors torque control," *IEEE Trans. Power Electron.*, vol. 17, no. 5, pp. 779–787, Sep. 2002.

[3] H. Kubota and K. Matsuse, "Speed sensorless field-oriented control of induction motor with rotor resistance adaptation," *IEEE Trans. Ind. Appl.*, vol. 30, no. 5, pp. 1219–1224, Sep./Oct. 1994.

[4] X. Zhang, B. Hou, and Y. Mei, "Deadbeat predictive current control of permanent-magnet synchronous motors with stator current and disturbance observer," *IEEE Trans. Power Electron.*, vol. 32, no. 5, pp. 3818–3834, May 2017.

[5] X. Yuan, S. Zhang, and C. Zhang, "Improved model predictive current control for SPMSM drives with parameter mismatch," *IEEE Trans. Ind. Electron.*, vol. 67, no. 2, pp. 852–862, Feb. 2020.

[6] Y. Zuo, J. Mei, C. Jiang, and C. H. Lee, "Digital implementation of deadbeat-direct torque and flux control for permanent magnet synchronous machines in the M-T reference frame," *IEEE Trans. Power Electron.*, vol. 36, no. 4, pp. 4610–4621, Apr. 2021.

[7] R. D. Lorenz and D. B. Lawson, "Performance of feedforward current regulators for field-oriented induction machine controllers," *IEEE Trans. Ind. Appl.*, vol. IA-23, no. 4, pp. 597–602, Jul. 1987.

[8] D.-C. Lee, S.-K. Sul, and M.-H. Park, "High performance current regulator for a field-oriented controlled induction motor drive," *IEEE Trans. Ind. Appl.*, vol. 30, no. 5, pp. 1247–1257, Sep./Oct. 1994.

[9] F. B. Del Blanco, M. W. Degner, and R. D. Lorenz, "Dynamic analysis of current regulators for ac motors using complex vectors," *IEEE Trans. Ind. Appl.*, vol. 35, no. 6, pp. 1424–1432, Nov./Dec. 1999.

[10] H. Kim and R. D. Lorenz, "Synchronous frame PI current regulators in a virtually translated system," in *Proc. 39th IAS Annu. Meeting Conf. Rec. IEEE Ind. Appl. Conf.*, 2004, pp. 856–863.

[11] X. Yuan and C. H. T. Lee, "A simple three-degree-of-freedom digital current controller with dead beat response for AC machines," *IEEE Trans. Ind. Electron.*, vol. 69, no. 8, pp. 7848–7858, Aug. 2022, doi: 10.1109/TIE.2021.3109540.

[12] K. H. Ang, G. Chong, and Y. Li, "PID control system analysis, design, and technology," *IEEE Trans. Control Syst. Technol.*, vol. 13, no. 4, pp. 559–576, Jul. 2005.

[13] K.-K. Huh and R. D. Lorenz, "Discrete-time domain modeling and design for AC machine current regulation," in *Proc. IEEE Ind. Appl. Annu. Meeting*, 2007, pp. 2066–2073.

[14] H. Kim, M. W. Degner, J. M. Guerrero, F. Briz, and R. D. Lorenz, "Discrete-time current regulator design for AC machine drives," *IEEE Trans. Ind. Appl.*, vol. 46, no. 4, pp. 1425–1435, Jul./Aug. 2010.

[15] S.-C. Yang and G.-R. Chen, "High-speed position-sensorless drive of permanent-magnet machine using discrete-time EMF estimation," *IEEE Trans. Ind. Electron.*, vol. 64, no. 6, pp. 4444–4453, Jun. 2017.

[16] Y. Yao, Y. Huang, F. Peng, J. Dong, and H. Zhang, "An improved deadbeat predictive current control with online parameter identification for surface-mounted PMSMs," *IEEE Trans. Ind. Electron.*, vol. 67, no. 12, pp. 10145–10155, Dec. 2020.

[17] B.-H. Bae and S.-K. Sul, "A compensation method for time delay of full-digital synchronous frame current regulator of PWM AC drives," *IEEE Trans. Ind. Appl.*, vol. 39, no. 3, pp. 802–810, May/Jun. 2003.

[18] J.-S. Yim, S.-K. Sul, B.-H. Bae, N. R. Patel, and S. Hiti, "Modified current control schemes for high-performance permanent-magnet ac drives with low sampling to operating frequency ratio," *IEEE Trans. Ind. Appl.*, vol. 45, no. 2, pp. 763–771, Mar./Apr. 2009.

[19] N. Hoffmann, F. W. Fuchs, M. P. Kazmierkowski, and D. Schröder, "Digital current control in a rotating reference frame-part i: System modeling and the discrete time-domain current controller with improved decoupling capabilities," *IEEE Trans. Power Electron.*, vol. 31, no. 7, pp. 5290–5305, Jul. 2016.

[20] A. Altomare, A. Guagnano, F. Cupertino, and D. Naso, "Discrete-time control of high-speed salient machines," *IEEE Trans. Ind. Appl.*, vol. 52, no. 1, pp. 293–301, Jan./Feb. 2016.

[21] M. Hinkkanen, H. A. A. Awan, Z. Qu, T. Tuovinen, and F. Briz, "Current control for synchronous motor drives: Direct discrete-time pole-placement design," *IEEE Trans. Ind. Appl.*, vol. 52, no. 2, pp. 1530–1541, Mar./Apr. 2016.

[22] A. G. Yepes, A. Vidal, J. Malvar, O. López, and J. Doval-Gandoy, "Tuning method aimed at optimized settling time and overshoot for synchronous proportional-integral current control in electric machines," *IEEE Trans. Power Electron.*, vol. 29, no. 6, pp. 3041–3054, Jun. 2014.

[23] A. G. Yepes, J. Doval-Gandoy, and H. Toliyat, "Disturbance rejection enhancement for three-phase converters by active inductance," in *Proc. 44th Annu. Conf. IEEE Ind. Electron. Soc.*, 2018, pp. 1176–1181.

[24] S. N. Vukosavic, L. S. Peric, and E. Levi, "Digital current controller with error-free feedback acquisition and active resistance," *IEEE Trans. Ind. Electron.*, vol. 65, no. 3, pp. 1980–1990, Mar. 2018.

[25] J.-W. Choi and S.-K. Sul, "Inverter output voltage synthesis using novel dead time compensation," *IEEE Trans. Power Electron.*, vol. 11, no. 2, pp. 221–227, Mar. 1996.

[26] G. Pellegrino, R. I. Bojoi, P. Guglielmi, and F. Cupertino, "Accurate inverter error compensation and related self-commissioning scheme in sensorless induction motor drives," *IEEE Trans. Ind. Appl.*, vol. 46, no. 5, pp. 1970–1978, Sep./Oct. 2010.

[27] S. Amarir and K. Al-Haddad, "A modeling technique to analyze the impact of inverter supply voltage and cable length on industrial motor-drives," *IEEE Trans. Power Electron.*, vol. 23, no. 2, pp. 753–762, Mar. 2008.

Xin Yuan (Member, IEEE) received the B.S. degree from Beijing Union University, Beijing, China, in 2013, and the M.S. degree from the North China University of Technology, Beijing, China, in 2016, and the Ph.D. degree in electrical engineering from the Beijing Institute of Technology, Beijing, China, in 2020.

He is currently a Research Fellow with the School of Electrical and Electronic Engineering, Nanyang Technological University, Singapore. He was a Research Associate with PEMC Group, University of Nottingham, Nottingham, U.K., from 2019 to 2020. His research interests include ac motor drives, power converters, multiphase motor drives, and fault-tolerant strategy of motor.

Jie Mei (Member, IEEE) received the B.S. degree from the School of Electrical and Computer Engineering, Georgia Institute of Technology, Atlanta, GA, USA, in 2015, and the Ph.D. degree from the Department of Electrical Engineering and Computer Science, Massachusetts Institute of Technology, Cambridge, MA, USA, in 2021, both in electrical engineering.

He is currently a Research Specialist with the Department of Electrical Engineering and Computer Science, Massachusetts Institute of Technology. His research interests include electric machines, multienergy systems, and electric vehicle technologies.

Jiahao Chen (Member, IEEE) received the B.Sc. and Ph.D. degrees in electrical engineering from Zhejiang University, Hangzhou, China, in 2014 and 2019, respectively.

In 2018, he was a Visiting Scholar, for one year, with the University of Wisconsin-Madison, Madison, WI, USA, where he was involved in bearingless motors. He is currently a Postdoctoral Research Fellow with Nanyang Technological University, Singapore. His research interests include electric machines, drives, and direct-drive technologies.

Yuefei Zuo (Member, IEEE) received the B.Sc. and Ph.D. degrees in electrical engineering and automation from the Nanjing University of Aeronautics and Astronautics, Nanjing, China, in 2010 and 2016, respectively.

He has been working as a Lecturer with Jiangsu University, Zhenjiang, China, since 2016. He is currently a Postdoctoral Research Fellow with the School of Electrical and Electronic Engineering, Nanyang Technological University, Singapore. His research interests include power electronics, electric machines and drives, and advanced control strategies.

Christopher H. T. Lee (Senior Member, IEEE) received the B.Eng. (First Class Hons.) and Ph.D. degrees in electrical engineering from the Department of Electrical and Electronic Engineering, The University of Hong Kong, Hong Kong, in 2009 and 2016, respectively.

He currently serves as an Assistant Professor with Nanyang Technological University, Singapore, and an Honorary Assistant Professor with The University of Hong Kong. He was a Postdoctoral Fellow and then a Visiting Assistant Professor with the Massachusetts Institute of Technology, Cambridge, MA, USA. His research interests include electric machines and drives, renewable energies, and electromechanical propulsion technologies. In these areas, he has authored or coauthored 1 book, 3 book chapters, and more than 100 refereed papers.

Dr. Lee is an Associate Editor for the IEEE TRANSACTIONS ON INDUSTRIAL ELECTRONICS, IEEE TRANSACTIONS ON ENERGY CONVERSION, *IEEE Access*, and *IET Renewable Power Generation*. He is a Chartered Engineer in Hong Kong. He is the recipient of many awards, including NRF Fellowship, Nanyang Assistant Professorship, Li Ka Shing Prize (the best Ph.D. thesis prize), and Croucher Foundation Fellowship.